

RESEARCH ARTICLE

Automatic oculomotor nerve identification based on data-driven fiber clustering

Jiahao Huang^{1,2}  | Mengjun Li^{3,4}  | Qingrun Zeng^{1,2}  | Lei Xie^{1,2} | Jianzhong He^{1,2} | Ge Chen⁴ | Jiantao Liang⁴ | Mingchu Li⁴ | Yuanjing Feng^{1,2}

¹Institute of Information Processing and Automation, College of Information Engineering, Zhejiang University of Technology, Hangzhou, China

²Zhejiang Provincial United Key Laboratory of Embedded Systems, Hangzhou, China

³Department of Radiology, Second Xiangya Hospital, Central South University, Hunan, China

⁴Department of Neurosurgery, Capital Medical University Xuanwu Hospital, Beijing, China

Correspondence

Yuanjing Feng, Institute of Information Processing and Automation, College of Information Engineering, Zhejiang University of Technology, Hangzhou 310023, China. Email: fyjing@zjut.edu.cn

Mingchu Li, Department of Neurosurgery Capital Medical University Xuanwu Hospital, No.45 Changchun Street, Xicheng District, Beijing 100053, China. Email: mingchu_li@xwhosp.org

Funding information

Key Projects of Natural Science Foundation of Zhejiang Province, Grant/Award Number: LZ21F030003; Key Research and Development Project of Zhejiang Province, Grant/Award Number: 2020C03070; National Natural Science Foundation of China, Grant/Award Number: 61976190; Natural Science Foundation of Zhejiang Province, Grant/Award Number: LQ21F020017

Abstract

The oculomotor nerve (OCN) is the main motor nerve innervating eye muscles and can be involved in multiple inflammatory, compressive, or pathologies. The diffusion magnetic resonance imaging (dMRI) tractography is now widely used to describe the trajectory of the OCN. However, the complex cranial structure leads to difficulties in fiber orientation distribution (FOD) modeling, fiber tracking, and region of interest (ROI) selection. Currently, the identification of OCN relies on expert manual operation, resulting in challenges, such as the carries high clinical, time-consuming, and labor costs. Thus, we propose a method that can automatically identify OCN from dMRI tractography. First, we choose the multi-shell multi-tissue constraint spherical deconvolution (MSMT-CSD) FOD estimation model and deterministic tractography to describe the 3D trajectory of the OCN. Then, we rely on the well-established computational pipeline and anatomical expertise to create a data-driven OCN tractography atlas from 40 HCP data. We identify six clusters belonging to the OCN from the atlas, including the structures of three kinds of positional relationships (pass between, pass through, and go around) with the red nuclei and two kinds of positional relationships with medial longitudinal fasciculus. Finally, we apply the proposed OCN atlas to identify the OCN automatically from 40 new HCP subjects and two patients with brainstem cavernous malformation. In terms of spatial overlap and visualization, experiment results show that the automatically and manually identified OCN fibers are consistent. Our proposed OCN atlas provides an effective tool for identifying OCN by avoiding the traditional selection strategy of ROIs.

KEYWORDS

data-driven, diffusion magnetic resonance imaging, fiber clustering, neurosurgery, oculomotor nerve, tractography

1 | INTRODUCTION

The oculomotor nerve (OCN) consists of somatic and parasympathetic nerves and plays a key role in the eye movements and pupil

Jiahao Huang and Mengjun Li authors contributed equally to this work.

This is an open access article under the terms of the Creative Commons Attribution-NonCommercial License, which permits use, distribution and reproduction in any medium, provided the original work is properly cited and is not used for commercial purposes.

© 2022 The Authors. *Human Brain Mapping* published by Wiley Periodicals LLC.

contractions by controlling extraocular muscles, ciliary muscles, and sphincter pupillae (Condos, 2021; Park, Rha, Lee, Chough, & Joo, 2017). The intramesencephalic segment of OCN extends from the oculomotor nuclear complex (ONC), which is ventral to the periaqueductal gray, and travels to the interpeduncular fossa (Brazis, Masdeu, & Biller, 2012; Condos, 2021). The cisternal segment of OCN travels outward and downward to the cavernous sinus and enters the orbits in the direction of the cavernous sinus parallel to the cavernous part of the internal carotid (Liang et al., 2009; as shown in Figure 1). OCN can be affected by many diseases, such as external brain injury (Nakagawa, Toda, Shibao, & Yoshida, 2017), congenital OCN palsy (Yang, Kim, & Hwang, 2020), and brain tumors (Inoue, Hashiguchi, Moroki, & Tokuda, 2020; Li et al., 2018; Taniguchi et al., 2018). Research (Tam, Lonngi, & Demer, 2018; Zhao, Li, Chang, Wang, & Sun, 2021) suggested that identifying the location of OCN is important in guiding diseases that involve the OCN.

Tractography based on diffusion magnetic resonance imaging (dMRI) can reveal the trajectory of OCN in three-dimensional, including the intramesencephalic and cisternal segments (Basser, Mattiello, & LeBihan, 1994; Gong et al., 2009; Hodaie, Quan, & Chen, 2010; Yoshino et al., 2016) which has been widely used in OCN identification to obtain the three dimensional (3D) relationship with surrounding structures (Jacquesson et al., 2019; Li et al., 2018; Muhammad & Niemelä, 2019). Hodaie et al. (2010) used dMRI data with the single-region of interest (ROI) selection method (cisternal segment of OCN) and diffusion tensor imaging (DTI) to reconstruct OCN. Results showed that the OCN terminates in the ONC or extends down the brainstem. Yoshino et al. (2016) used high-definition fiber tractography and two-ROI selection method (fourth ventricle at the level of upper pons and cisternal segment) to identify OCN fibers in healthy subjects and patients with brain tumors and presented similar

results. Previous studies (Hodaie et al., 2010; Yoshino et al., 2016) identified putative OCN fibers through manually placed ROIs. However, common tractography methods have difficulty in tracking the complete OCN pathway because of the elongated structure of the OCN, cerebrospinal fluid (CSF) where the cisternal segment of OCN is infiltrated, and partial volume effect (Jacquesson et al., 2019; Maier-Hein et al., 2017). Therefore, experts should place the ROI manually to promote OCN tractography and identification. (1) The identification of the OCN is sensitive to the ROI placement, and manual ROI selection methods suffer from imaging artifacts and/or noise and operator bias. Thus, the selection of the best-performing ROIs remains a challenge (Wu et al., 2018; Zhang et al., 2020). (2) Manually placing ROIs is laborious, time-consuming, and unfriendly to beginners who suffer from lack of knowledge in anatomy (Jacquesson, Yeh, et al., 2019; Xie et al., 2020).

Automatic identification methods are proposed to avoid the pitfalls of traditional ROI selection methods. The automatic identification based on cortical parcellation (Sporns, Tononi, & Kötter, 2005; Wassermann et al., 2016) allows for highly specific identification but leads to the low sensitivity of tract identification and effects from individual anatomical variations (Bonilha et al., 2015). Many methods based on atlas and shape models, which emphasize the use of statistical shape or statistical appearance, have been proposed to identify cranial nerves (Sultana, 2017). However, these methods cannot identify the nerve course of the intramesencephalic segment. Another type of method can identify by registering ROI templates in standard onto individual information for tractography fiber selection (Malinsky et al., 2013). However, such ROI-based methods rely on the accuracy of the registration algorithm. When squeezed by tumors, cranial nerves are displaced. Common ROI templates are no longer applicable, resulting in recognition failure (Chen et al., 2011; Jacquesson, Yeh,

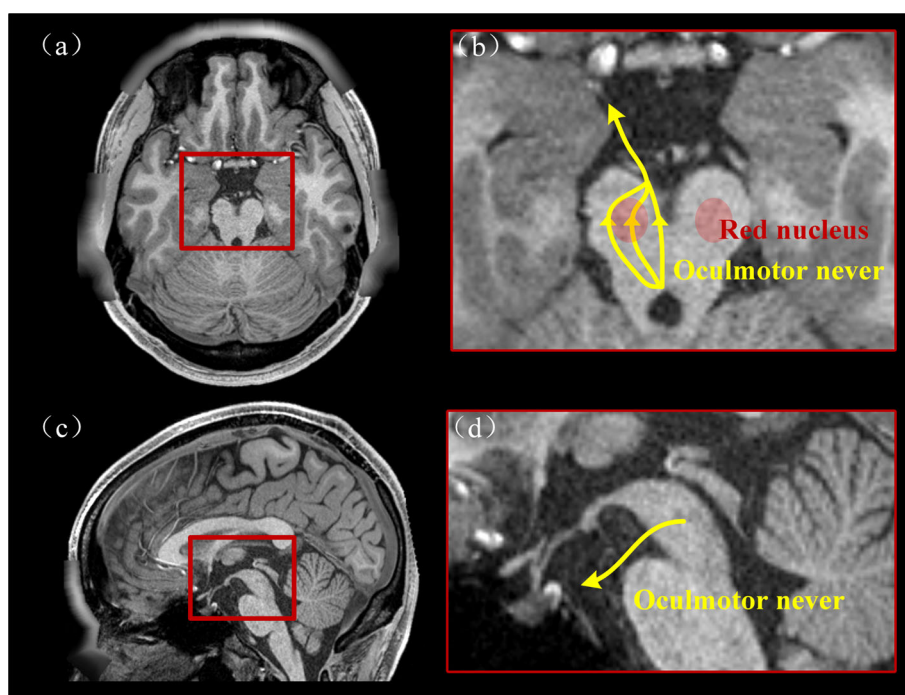


FIGURE 1 Schematic anatomical overview of the oculomotor nerve (OCN). (a) The transverse plane of the T1-weighted MR image at the level of the midbrain. (b) The details of (a). (c) The sagittal plane of the T1-weighted MR image. (d) The details of (c)

et al., 2019). Moreover, ROI-based methods are sensitive to tractography methods that require multiple ROIs to be constrained. In contrast to other methods, the dMRI tractography atlas uses a distinct white matter connectivity modeling assumption to group fibers with comparable trajectories into clusters. These studies successfully demonstrated the automated identification of anatomical white matter fiber tracts (Wu et al., 2018; Zhang et al., 2020) (e.g., trigeminal nerve and white matter tracts), which achieve in escape from individual differences including objects, time, locations, and experimental conditions (Fischl, 2012; O'Donnell et al., 2017), with several advantages as follows. (1) Fiber tracts can be automatically identified with high consistency across subjects and augmented with anatomical annotations (Wu et al., 2018). (2) The automatic identification method uses only dMRI data, obviating the need for inter-modality registration (Zhang et al., 2020). (3) After the atlas creation, the subject-specific automatic identification does not require the user to have extensive knowledge of anatomy.

This article aims to enable the automated identification of the OCN in new tractography data slipping the leash of ROI-based methods. We have compared the performance of multiple tractography methods and different parameters to find suitable strategies for OCN tractography. Then, an anatomically curated OCN atlas is created by relying on fiber clustering. We have used this fiber clustering pipeline to identify common OCN structures in an atlas population, including 40 subjects from the Human Connectome Project (HCP; Van Essen et al., 2013). On the basis of the anatomical knowledge of experts, we finally identify six clusters belonging to OCN. Each cluster of OCN in the atlas represents a certain OCN anatomical subdivision and variability in the population. The established OCN atlas contains OCN fibers, which exist three kinds of positional relationships with the red nuclei and two kinds of positional relationships with medial longitudinal fasciculus (MLF; the fibers that OCN connects to MLF called OCNM fibers; Kwon, Kim, Kim, & Jang, 2013; Li et al., 2021; Miller, Mark, Ho, & Haughton, 1997; Vitošević et al., 2013). Finally, we have applied the proposed atlas to identify the OCN of the new 40 subjects. Results show that the automatic identification of OCN by our proposed strategy is quantitatively and qualitatively consistent with the findings of ROIs manually placed by an expert. The OCN is dissimilar from the trigeminal nerve and white matter tracts and is more elongated, resulting in the strict selection of methods and parameters (including tractography parameters, ROI, and similarity) in tractography and atlas generation. After creating the atlas, we have successfully applied the OCN atlas to patients with brainstem cavernous malformation (BSCM). We have accurately identified the OCN, which surrounds the BSCM and the 3D positional relationship between OCN and surrounding tissues.

In the rest of this article, we describe our proposed methods, that is, OCN atlas creation and automatic OCN identification. Then, we demonstrate an application to dMRI datasets from two different acquisition sites, including HCP dataset and two patient data with BSCM. Finally, the OCN identification performance of our proposed method is evaluated quantitatively and qualitatively and compared with the method in which the expert selects the OCN.

2 | METHODS

2.1 | Data acquisition and preprocessing

Ninety HCP subjects are used in this work, 10 of which are to compare multiple tractography methods and parameters, 40 to generate OCN atlas, and the remaining 40 to validate the proposed method. In addition, we apply the proposed method to two BSCM patients with brainstem tumors. The follows are the detailed parameters and preprocessing:

2.1.1 | HCP dataset

The HCP provides high-quality dMRI and T1-weighted (T1w) data, which are approved by the local Institutional Review Board of Washington University. The dMRI acquisition parameters in HCP are as follows: TR = 5,520 ms; TE = 89.5 ms; FA = 78°; voxel size = $1.25 \times 1.25 \times 1.25 \text{ mm}^3$; FOV = $210 \times 180 \text{ mm}^2$; *b*-values = 1,000, 2,000, and 3,000 s/mm²; and 90, 90, and 90 diffusion sampling directions. The T1w acquisition parameters in HCP are as follows: TR = 2,400 ms; TE = 2.14 ms; and voxel size = $0.7 \times 0.7 \times 0.7 \text{ mm}^3$. Detailed information about the HCP data acquisition and preprocessing can be found in <http://www.humanconnectomeproject.org/> (Glasser et al., 2013).

2.1.2 | The BSCM patient data

The MRI data of the patient with tumor are acquired at Xuanwu Hospital Capital Medical University by using the Siemens Skyra 3T scanner. dMRI acquisition parameters in tumor patient data are: TR = 8,900 ms, TE = 95 ms, *b*-values = 1,000 s/mm², 60 diffusion sampling directions, and voxel size = $2.2 \times 2.2 \times 2.2 \text{ mm}^3$. The T1w image acquisition parameters in the data of patient with tumor are as follows: TR = 2,400 ms; TE = 2.27 ms; 192 slices; FOV = 250 mm^2 ; and voxel size = $1.0 \times 1.0 \times 1.0 \text{ mm}^3$. Written informed consent forms are signed by all subjects, and the ethics committee at Xuanwu Hospital, Capital Medical University has given its permission before testing.

2.1.3 | Data processing

We design a series of processing pipelines, including motion correction, denoising, and eddy current correction. First, we apply denoising and eddy correction on dMRI and denoising on T1w images (Tournier et al., 2019).

Second, the automated reconstruction and labeling of cortical and subcortical regions are performed using the Freesurfer (Fischl, 2012) on T1w images. The seed imaging and regions of avoidance (ROAs) are chosen by automatically extracting the corresponding numbered brain area. We set the whole brainstem as the seed imaging (as shown in Figure 2). In terms of anatomical considerations, the anatomical pathway of the OCN originates from the ONC which is located in the

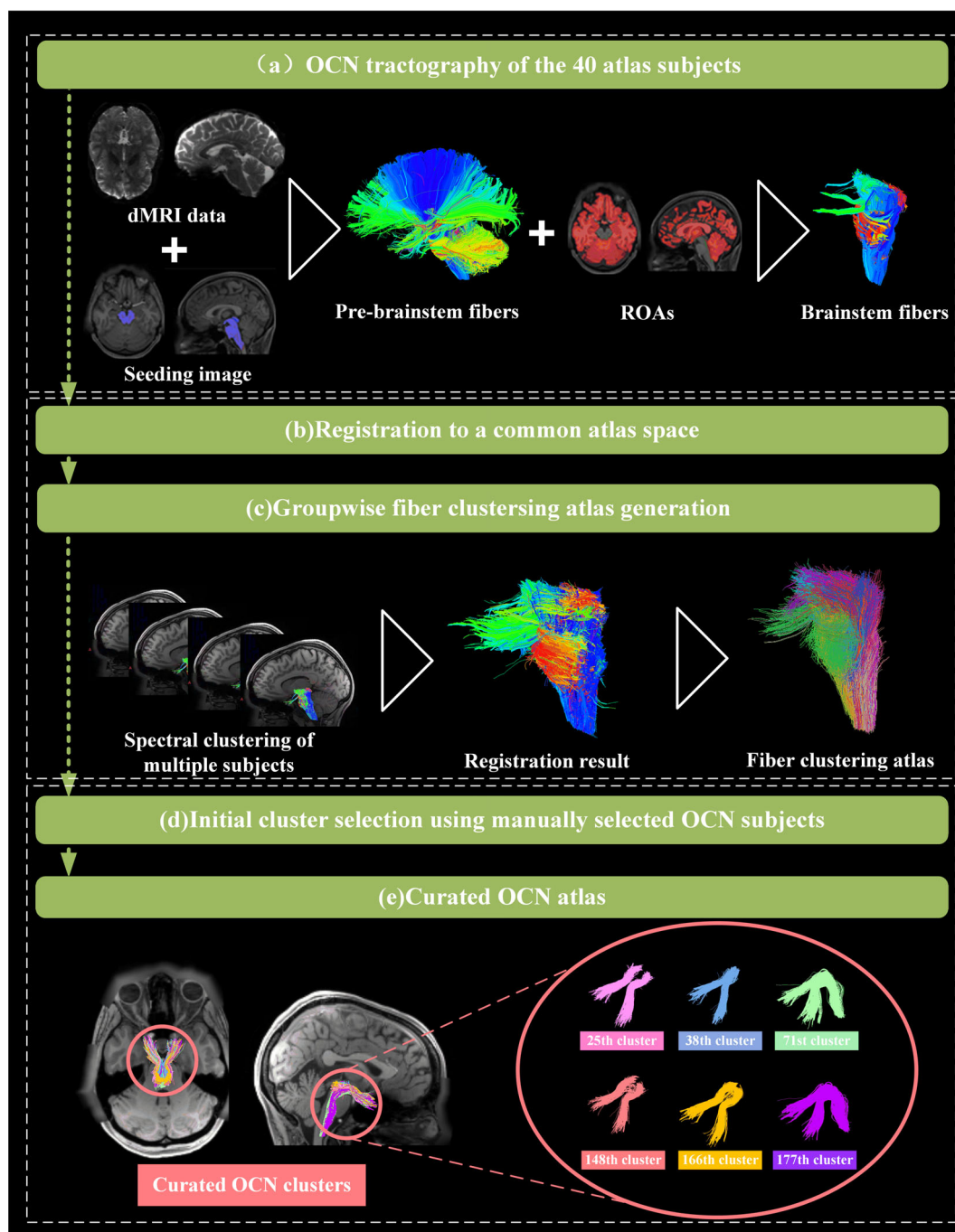


FIGURE 2 Oculomotor nerve (OCN) atlas generation. (a) OCN tractography performs under the constraints of region of avoidance (ROA) and seed imaging. (b) Registration of 40 subject brainstem fibers to a common atlas space. (c) Spectral clustering for the generation of a fiber clustering atlas by using the brainstem fibers from 40 atlas subjects. (d,e) Manual selection of OCN subjects through initial cluster selection on the basis of expert anatomical experience. Six clusters, including OCN (four clusters) and OCNM (two clusters), are identified to belong to OCN on the basis of expert neuroanatomical knowledge

central and dorsal midbrain (Brazis et al., 2012; Condos, 2021). Then OCN crosses the ventral midbrain and enters the cistern from the outer edge of the interpeduncular fossa (Park et al., 2017). And the rest of the brain regions (i.e., the whole brain excepts brainstem) are used as (ROAs. Because the pathway of the cisternal segment of OCN does not enter any other brain areas (Park et al., 2017).

2.2 | Comparison of multiple tractography and parameters

Tractography methods are widely used in cranial nerve studies (Behan et al., 2017; Castellaro et al., 2020; He et al., 2021; Hodaie et al., 2010). To find a better method for OCN reconstruction, we

compare the performance of three different direction estimation methods including constraint spherical deconvolution (CSD; Behan et al., 2017; Tournier, Calamante, & Connelly, 2012), multi-shell multi-tissue constraint spherical deconvolution (MSMT-CSD), and DTI (Hodaie et al., 2010) to reconstruct the 3D trajectory of OCN. In contrast to CSD and DTI, MSMT-CSD is utilized to fit a five-tissue-type segmented tissue image by using multiple b -values for the multi-type tissue fiber orientation distribution (FOD; Castellaro et al., 2020; Jeurissen, Tournier, Dhollander, Connelly, & Sijbers, 2014). To describe the complete OCN pathway, we prepare a careful plan for each method, including the seed imaging, ROAs, and parameters.

2.2.1 | Parameters

We conduct an experiment to determine the best-performing parameters of each tractography method for OCN tractography. FA threshold values of 0.05, 0.1, and 0.15 and angle threshold values of 30° , 60° , and 90° are used. The remaining parameters are kept constant and set as follows: number of streamlines = 500,000; step size = 0.5 mm; and minimum length = 20 mm.

2.2.2 | The standards of OCN fiber selection

Experts manually identify OCN fibers and OCNM fibers from tractography fibers generated by three tractography methods. The first ROI (cisternal segment of the OCN as illustrated in Figure 3; Hodaie et al., 2010) is used to confirm preliminary OCN fibers and OCNM fibers. Then, OCN fibers and OCNM fibers are distinguished

by placing the ROI or ROA at the region of the tegmentum of pons as illustrated in Figure 3. Finally, results are further identified separately. Fibers with significantly different intramesencephalic segment of OCN orientation from anatomical knowledge and fibers with incorrect orientations of the cisternal segment are excluded.

2.2.3 | Anatomical assessment criteria of the OCN

We evaluate the multi-method multi-parameter tractography results in the following two aspects. (a) The pathway of OCN fibers and OCNM fibers goes through the correct anatomical location. (b) The lengths of the cisternal segment of the OCN are sorted on the basis of conforming to the anatomical position of OCN. A long cisternal segment of the OCN indicates that the combination of parameters and method has improved performance in OCN reconstruction. We first determine the optimal parameters for each tractography method and perform a cross-method comparison to determine the best combination of method and parameters for OCN tractography performance. Tractography methods and parameters are used as the basis for subsequent atlas and test subjects.

2.2.4 | Reconstruction rate of OCN subdivisions

We assess the ability of each tractography method to reconstruct the two subdivisions of the OCN successfully. Specifically, we consider that the fiber pathway is successfully traced if at least one fiber is retained on both sides and each OCN anatomical subdivision is successfully reconstructed fibers after ROI selection (i.e., OCN and

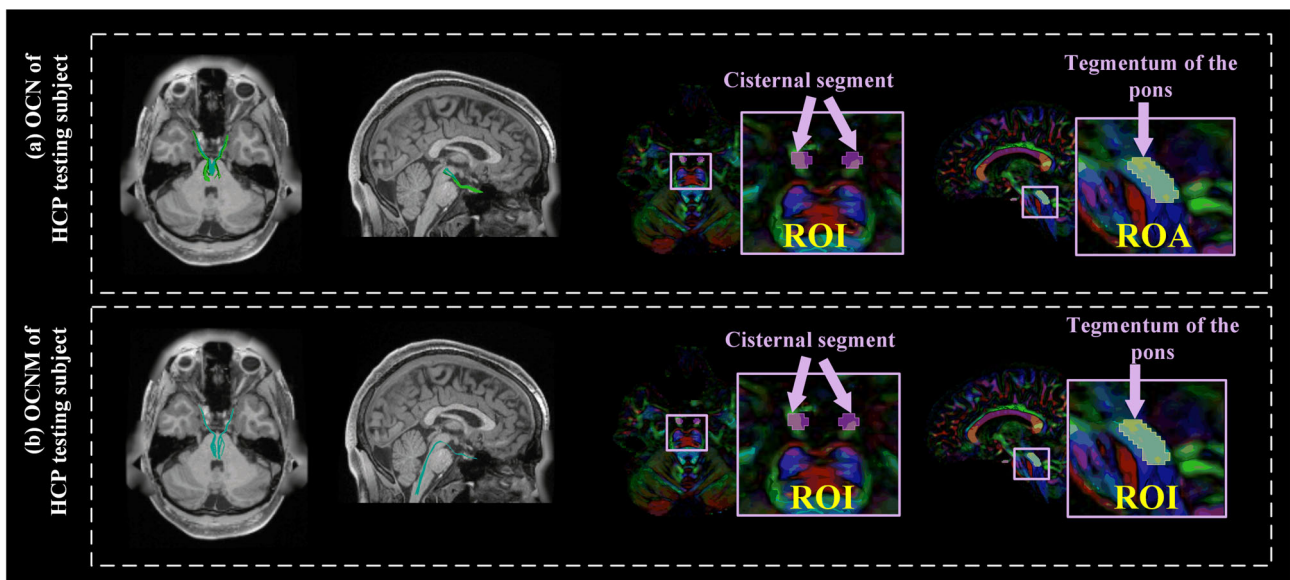


FIGURE 3 Region of interest (ROI) and region of avoidance (ROA) for OCN and OCNM selection. (a) ROI (cisternal segment of oculomotor nerve [OCN]) and ROA (tegmentum of the pons) for OCN selection. (b) OCNM selection differing from OCN selection only in the tegmentum of the pons used as ROI. Note that, in order to show complete OCN, the location of the slice chose from T1 anatomical image maybe lower (or further back) than the position of OCN

OCNM). So, we compute the overall reconstruction rate for the full OCN pathway (i.e., the percentage of subjects where both subdivisions are successfully reconstructed).

2.3 | OCN atlas generation

We first determine the optimal parameters for each tractography method and then perform a cross-method comparison to determine the best combination of method and parameters for OCN tractography performance. The tractography methods and parameters are used as the basis for subsequent atlas and test subjects.

2.3.1 | Generation of OCN fiber clustering atlas

We learn a data-driven model of common OCN structure in humans through the following processes:

OCN tractography of atlas subjects

We acquire pre-brainstem fibers from 40 atlas subjects. Each atlas subject tractography is performed with the best-performance tractography strategy (i.e., MSMT-CSD, angle threshold of 45, and FA threshold of 0.05). Then individual brainstem fibers are produced after removing invalid fibers passing through ROAs to reduce memory space and computational cost as illustrated in Figure 2a.

Multi-subject fibers registration

In a multiscale way, we compute an unbiased entropy-based groupwise tractography registration (O'Donnell, Wells, Golby, & Westin, 2012; Zhang et al., 2020) of brainstem tractography from each subject after individual OCN tractography, as illustrated in Figure 2b. The registration employs 20,000 fibers from each subject for a total of 800,000 fibers, with a minimum fiber length of 45 mm, and affine then coarse-to-fine b-spline registration with multiscale sigma values from 20 down to 2 mm and a final b-spline grid size of $8 \times 8 \times 8$. After registration, an OCN tractography with high density and good spatial correspondence is produced.

Spectral clustering

OCN tractography data are divided into K clusters by spectral clustering to create a high-dimensional fiber clustering atlas (O'Donnell & Westin, 2007), in which K is a user-supplied parameter that defines the parcellation scale. First, many tractography fibers are highly similar to their neighboring fibers on the basis of anatomy (Presseau, Jodoin, Houde, & Descoteaux, 2015). Thus, we perform a random sampling of 20,000 fibers from each subject rather than analyzing all fibers across subjects and ensure that the extracted number of fibers is sufficient to represent the anatomical structure of the OCN in the population. Then, we implement groupwise spectral embedding and clustering to divide OCN tractography fibers. The groupwise spectral embedding creates an independent spectral space that represents similarity information

between fibers. In addition, we use a random sampling method called Nystrom (Fowlkes, Belongie, Chung, & Malik, 2004) to represent the space compactly and remarkably reduce the number of fiber distance calculations in the subsequent steps. Four iterations (over two standard deviations from the cluster's mean fiber affinity) are performed to remove improbable fibers for cluster consistency in the atlas (O'Donnell et al., 2017; O'Donnell & Westin, 2007).

We generate multiple OCN atlases (as shown in Figure S1) of different scales by setting different K values ($K = 100, 200, 500,$ and $1,000$). Our study does not consider an increased number of fiber clusters because a detailed scale remarkably increases the computation time and complexity. It can sort out the fiber clusters of OCN and OCNM when the atlas chooses a coarse classification scale ($K = 100$) but contains many false-positive fibers. When we choose a small classification scale ($K = 200$), fiber clusters belonging to the OCN hardly present false-positive fibers and differentiate the anatomical differences between the OCN and OCNM. In addition, when the classification scale is $K = 500$ and $1,000$, the lack of consistency in profiles across subjects and increased computing time are observed. In the end, we choose 200 clusters for the brainstem classification based on three considerations: anatomical correctness, the structural integrity of the OCN, and computational complexity.

2.3.2 | Supervision of OCN fiber clusters

Based on the experience of our previous work (Zeng et al., 2021), the OCN is present in multiple fiber clusters, and the integration of these fiber clusters can represent an anatomical subdivision of the complete OCN. We obtain the fixed atlas by subdividing multi-subject registered brainstem fibers into 200 clusters (clusters are labeled as 1–200). Then the professional anatomical expert (Mengjun Li) labels whether each cluster belongs to OCN or OCNM with T1w images. Another expert (Mingchu, Li who is a neuroanatomist) view the curated OCN or OCNM clusters and confirmed their anatomical correctness. The results show that the 25th, 38th, 148th, and 166th clusters from the atlas belong to the OCN, and 71st and 177th clusters from the atlas belong to the OCNM as illustrated in Figure 2c.

2.4 | OCN atlas evaluation

We use the proposed atlas to identify subject-specific OCN from 80 HCP subjects (40 HCP atlas subjects and 40 HCP testing subjects) and two BSCM patients. First, individual OCN fiber tractography is performed after the seed imaging and ROAs are extracted from the new data. Then, brainstem tractography of the new subject are registered to the OCN atlas space by using the affine and nonrigid transformation with 45,000 fibers from individual tractography and minimum fiber length of 45 mm as illustrated in Figure 4b. Third, subject-specific fiber clusters are detected using the spectral embedding of the registered tractography, and each fiber is assigned to the closest atlas cluster (Guevara et al., 2016; O'Donnell et al., 2017;

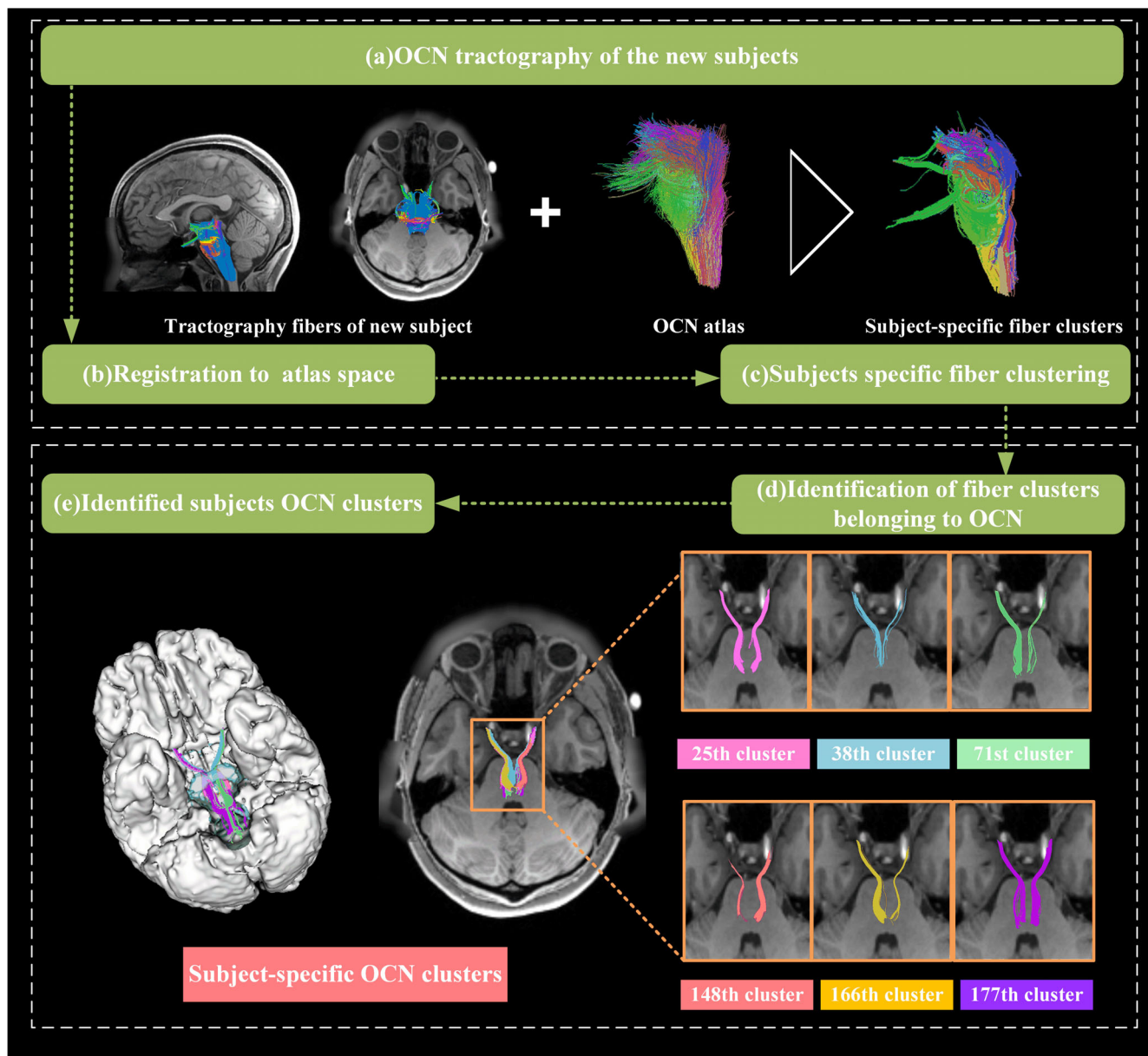


FIGURE 4 Individual oculomotor nerve (OCN) identification. (a) New subject performing OCN tractography in the same way as atlas subjects. (b) Registration of the individual OCN tractography data to the atlas space. (c) Fiber clustering of the individual tractography data in accordance with the fiber clustering atlas. (d–e) Identification of OCN clusters in the new subject is conducted by finding the corresponding subject-specific clusters to those annotated in the atlas

Zhang et al., 2020). After the tractography data of the new subject are divided into multiple fiber clusters, two iterations are performed to reject outlier fibers. In the end, OCN identification of the new subject is conducted by automatically finding the subject-specific clusters that corresponded to the annotated OCN clusters in the atlas (as shown in Figure S2). The OCN is present in six fiber clusters, where we select the 25th, 38th, 148th, and 166th clusters in the subject-specific atlas to form anatomically OCN fibers, and the 71st and 177th clusters to form anatomically OCNM fibers, as illustrated in Figure 4d,e. We perform the following work to evaluate the OCN identification performance of our method.

2.4.1 | OCN identification

We report the average identification rate of different anatomical subdivisions (OCN and OCNM) in 82 subjects (including 80 HCP subjects and 2 BSCM patients). First, two experts (Mengjun Li and Mingchu Li) perform anatomical confirmation of the OCN in each subject and subdivide its anatomy into OCN fibers and OCNM fibers. Specially, we define that if more than an OCN fiber or/and OCNM fiber of the subject is successfully identified, the atlas is valid for the subject. Then, we calculate the average percentage of successfully automatically identified OCN in HCP subjects.

2.4.2 | OCN spatial overlap

For spatial overlap, referring to the traditional segmentation task, we use the Accuracy (ACC), Sensitivity (SE), and Precision (PR) (Taha & Hanbury, 2015) to assess the ability of our method to identify correct OCN fibers of individual HCP subject. ACC, SE, and PR are defined as follows

$$ACC = \frac{TP + TN}{TN + TP + FP + FN} \quad (1)$$

$$SE = \frac{TP}{TP + FN} \quad (2)$$

$$PR = \frac{TP}{TP + FP} \quad (3)$$

in which TP, FP, TN, and FN denote the number of true-positive, false-positive, true-negative, and false-negative voxels of automatic identification OCN, respectively.

Then, we quantify the spatial overlap between manually and automatically identified OCN with the weighted Dice (wDice) coefficient (Cousineau et al., 2017; Dice, 1945). On the basis of the traditional Dice calculation method that is designed to calculate the fiber overlap, wDice sets high weights for voxels with high fiber density, which is also scientific and reasonable. We calculate the mean and standard deviation of wDice coefficients for 40 atlas subjects, 40 test subjects, and 2 BSCM patients.

In addition, to demonstrate the robustness of our proposed OCN atlas, we classify the brainstem tractography of the same subject five times based on the fixed atlas by clustering at the same scale. Then we visualize the identification OCN results for each spectral clustering. We use wDice (Cousineau et al., 2017; Dice, 1945) to quantitatively describe the consistency among each result and the similarity of each automatic identification result with the manual identification result.

2.4.3 | OCN visualization

We use the 3D Slicer to visualize the automatic and manual identification results of OCN and OCNM. Also, we show the relationship between OCN and OCNM and their surrounding tissues separately in 3D. In particular, for BSCM patients, we analyze the identification results in combination with their clinical symptoms. For BSCM patients whose lesions are located next to the OCN and cause corresponding clinical presentations, qualitative analysis is used to evaluate the displacement and/or disruption of the OCN in the lesion side through comparisons with the contralateral homologous OCN. Displacement is defined as a change in

the location or direction of the affected OCN due to the BSCM mass effect. Disruption is defined as thinning of the affected OCN, discontinuity in part of the affected OCN, or lack of visualization in most or all of its anatomy courses (Faraji et al., 2015; Lazar, Alexander, Thottakara, Badie, & Field, 2006; Li et al., 2018).

All of the software which are used in this project, including fiber tractography (<https://www.mrtrix.org>), computational tractography analysis methods (<https://github.com/SlicerDMRI/whitematteranalysis>), and tractography visualization with anatomical hierarchies in 3D Slicer (<http://www.slicer.org>), are open source.

3 | EXPERIMENTAL RESULTS

In the present study, we create an OCN atlas to identify the OCN automatically from new subjects. We perform the identification rate calculation, spatial overlap calculation, and the OCN visualization to demonstrate the reliability of our proposed automatic identification of the OCN atlas. First, we invite anatomical experts (Mengjun Li and Mingchu Li) to identify the OCN manually from brainstem fibers, which are obtained from 27 combinations with methods and parameters. The results of reconstruction rate (see Table 1) and visualization (see Figure 5) suggest that MSMT-CSD combined with deterministic tractography has the best pathway reconstruction performance for OCN reconstruction. Second, the OCN identification performance of our proposed method is evaluated quantitatively. The proposed OCN atlas has good identification rates and spatial overlap when using test subjects. Regarding the different subdivisions, OCN and OCNM are successfully identified using the proposed automated identification method in all subjects. The subjects that manual identifying failures are irrespective in our statistics. The average coverage rates (mean wDice) of automatic OCN and OCNM identification compared with those of expert manual selection are higher than 90.50%, and the mean wDice of OCN is higher than that of OCNM. Finally, the atlas is successfully used to identify OCN from tumor subjects, and we verify the identified results with the finding in surgery. We find that the automatic identification result is highly consistent with surgery findings.

3.1 | Assessment of the performance of tractography method for OCN reconstruction

3.1.1 | Anatomical assessment criteria of the OCN

Different parameters and direction estimation methods remarkably affect the performance of OCN tractography. In our study, we

TABLE 1 Reconstruction rate of OCN subdivisions for each tractography method

Methods	Best-performed tractography parameters	OCN	OCNM	Overall
DTI	FA = 0.15, angle = 60°	0%	0%	0%
CSD	FA = 0.10, angle = 60°	70%	50%	50%
MSMT-CSD	FA = 0.05, angle = 45°	100%	80%	80%

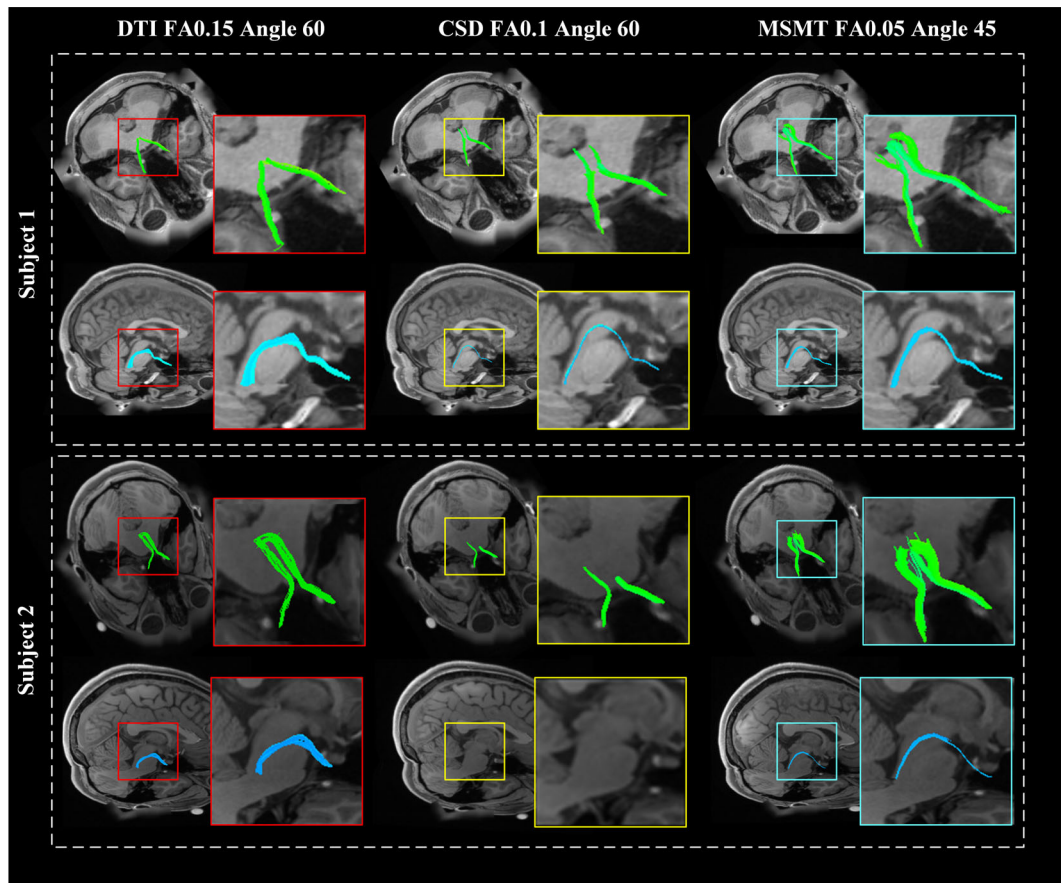


FIGURE 5 Visual comparison of the oculomotor nerve (OCN) reconstruction from three tractography methods. OCN fibers and OCNM fibers obtained from two HCP subjects are displayed and overlaid on the T1w image. The first box shows the results of OCN fibers, and the second box shows the results of OCNM fibers

compare 27 fiber tractography strategies for OCN identification from the same subject. We first choose the best-performing parameters for each method and perform cross-method comparisons. Figure 5 shows the pathways of OCN fibers and OCNM fibers from three methods, which are overlaid on the T1w image. We can find that the intramesencephalic segment of OCN obtained by DTI from Subject 1 stops at the brainstem prematurely. OCNM fibers obtained by DTI are error fibers that the pathway does not reach the location of the midbrain superior colliculus. The OCN fibers obtained by CSD contain only one positional relationship (pass between) with the red nuclei. In contrast to those obtained by DTI and CSD, the cisternal segments of OCN fibers and OCNM fibers obtained by MSMT-CSD are longer and more accurate. Moreover, the cisternal segment of OCN fibers is more intact to DTI and CSD.

3.1.2 | Reconstruction rate of OCN subdivisions

Table 1 shows the reconstruction rates of the two OCN subdivisions and the overall reconstruction rates across all subdivisions and all subjects. MSMT-CSD generates the highest overall

reconstruction rate, where two subdivisions are reconstructed in 8 of 10 subjects. This is followed by CSD, in which both subdivisions are reconstructed in 5 of 10 subjects. DTI performs the worst and completely identifies extremely few OCN fibers and OCNM fibers. After comprehensive consideration of visualization and reconstruction rates, MSMT-CSD is the most suitable method for OCN reconstruction.

3.2 | OCN identification rate

Table 2 gives the OCN identification rate of the overall OCN and its subdivisions obtained using the proposed automated identification method and the manual selection method. Regarding the different subdivisions, we obtain relatively high identification rates for OCN and OCNM in 40 HCP atlas subjects (average = 100.0%) and 33 HCP test subjects through the successful manual identification (average OCN identification rate = 96.97% and average OCNM identification rate = 100.0%). For subjects with BSCM, we identify respectively OCN fibers and OCNM fibers surrounding the lesion from different subjects.

TABLE 2 OCN identification rate (percentage of successfully identified OCN and OCNM fibers) of the overall OCN and its subdivisions using the proposed automated identification method and the manual selection method

Subjects	Overall		OCN		OCNM	
	Automatic (%)	Manual (%)	Automatic (%)	Manual (%)	Automatic (%)	Manual (%)
HCP atlas subjects (<i>n</i> = 40)	100	100	100	100	100	100
HCP testing subjects Successful manual identification (<i>n</i> = 33)	100	100	96.96	100	100	100
HCP testing subjects unsuccessful manual identification (<i>n</i> = 7)	–	–	–	–	–	–
BSCM patient 1	100	100	100	100	0	0
BSCM patient 2	100	100	0	0	100	100

TABLE 3 The quantitative comparison of automatic and manual results in terms of ACC, PR, and SE

Subjects	OCN			OCNM		
	ACC	PR	SE	ACC	PR	SE
HCP atlas subjects (<i>n</i> = 40)	0.9999	0.7215 ± 0.015	0.9325 ± 0.010	0.9999	0.7964 ± 0.021	0.8489 ± 0.016
HCP testing subjects successful manual identification (<i>n</i> = 33)	0.9999	0.7412 ± 0.014	0.9172 ± 0.018	0.9999	0.7966 ± 0.034	0.7965 ± 0.030

Note: All metrics are calculated based on the mean ± standard deviation of all successful manual identification subjects in HCP.

3.3 | OCN spatial overlap

Table 3. gives the quantitative comparison of automatic and manual results in terms of ACC, PR, and SE. In the experimental results, the mean ACC is close to 1. Because the number of voxels from the imaging data of a complete HCP subject is much greater than the number of voxels from gracile OCN fibers (i.e., TN is much larger than TP, FN, and TP). The higher mean SE shows that our proposed atlas can maximize the identification of OCN fibers from new individual subjects.

Table 4 gives the mean and standard deviation of wDice scores across 40 HCP atlas subjects and 33 HCP test subjects. For 2 BSCM patients, we only give wDice in Table 4. Average wDice scores >0.72 are an ideal outcome according to Cousineau et al. (2017). OCN fibers and OCNM fibers obtained from the OCN atlas are highly comparable

TABLE 4 Spatial overlap (wDice score) between automatically (proposed) and manually identified OCN fibers and OCNM fibers

Subjects	OCN	OCNM
40 HCP atlas subjects	0.9417 ± 0.0127	0.9371 ± 0.0444
33 HCP testing subjects with successful manual	0.9544 ± 0.0594	0.9050 ± 0.0675
BSCM patient 1	0.9913	0
BSCM patient 2	0	0.9307

to the manually identified OCN. Furthermore, the wDice coefficient demonstrates the accuracy of our approach.

The lowest wDice coefficient among the five clustering results is 0.9846 as illustrated in Figure 6d, which proves that the clustering results based on the fixed atlas from each spectral clustering are consistent. The results are also consistent with the manual identification by experts.

3.4 | OCN visualization

Figure 7a shows the overlap between the automatically and manually identified OCN fibers in 3D. OCN fibers and OCNM fibers from HCP subjects have high visual consistency and pass the corresponding anatomical position. OCN fibers emerge from the ONC and pass the VentralDC through the midbrain by the interpeduncular fossa as illustrated in Figure 7b. Figure 7a,c show that the MLF connecting OCN is consistent with its anatomy that is situated near the midline of the brainstem.

3.4.1 | Case 1

A 41-year-old man presents with a BSCM at the left midbrain. The left automatically visualized OCN, constructed from the OCN atlas, is displaced superiorly and medially by the BSCM. Disruption is not identified when compared to the contralateral automatically visualized

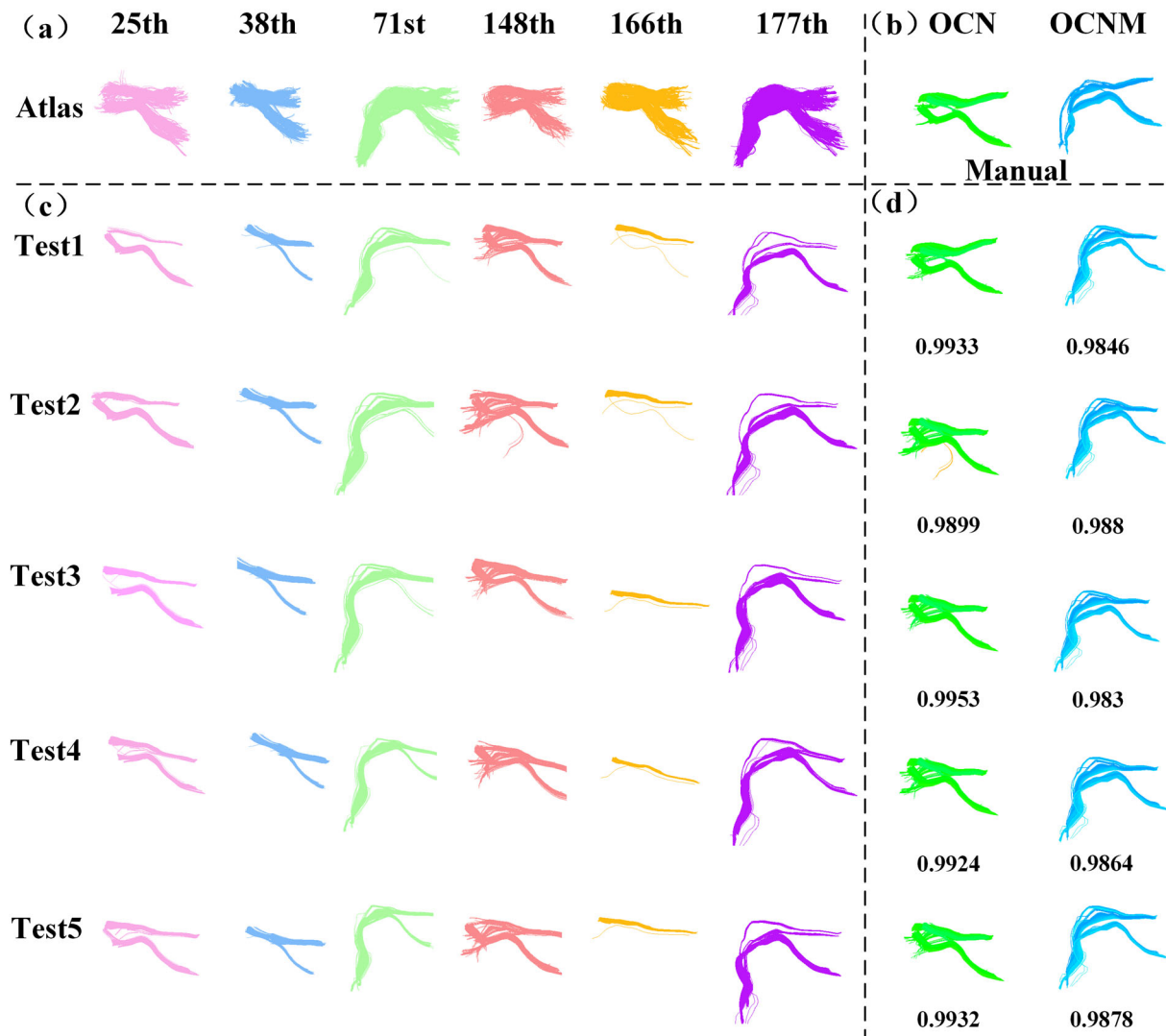


FIGURE 6 The results of the atlas stability test. (a) The clusters belonging to oculomotor nerve (OCN) and OCNM in the atlas. (b) Results of manual identification of individual subject-specific tractography. (c) Results of five separate clustering of the same data at the same scale. (d) Results of automatic identification of OCN and OCNM, and the quantitative analysis (wDice) of the comparison with the manual identification results are shown in figure

OCN. This patient has adduction dysfunction of the left eye, which could be caused by the displacement of the left OCN resulting from BSCM, the adduction dysfunction of the left eye is relieved after surgery (Figure 8).

3.4.2 | Case 2

A 42-year-old man presents with a BSCM at the right pons. Displacement is not observed in the right automatically visualized OCN constructed from the OCN atlas. The disruption is not identified when compared to the contralateral automatically visualized OCN. This patient has no motor dysfunction of the right OCN. However, this patient has ghosting and horizontal nystagmus, which could be caused by the displacement of the MLF resulting from BSCM (Figure 9).

4 | DISCUSSION

In this article, we propose an automatic OCN identification method to enable robust anatomical OCN identification from new subjects and investigate the patient whose tumor involves morphological changes in the OCN. We demonstrate the robustness and reliability of our method in identifying OCN by using a dataset of 80 HCP subjects and 2 BSCM patients. The automatic method provides an efficient tool for dMRI tractography to simple post processing without multiple ROIs selection and fiber filtering. Our overall observations are discussed below.

The proposed automatic OCN identification method successfully applies the subject-specific OCN identification, and the OCN of studied subjects is successfully identified 100% of the time. The results of automatic and manual identification methods are compatible and have a highly visually similar OCN trajectory and good spatial overlap. We

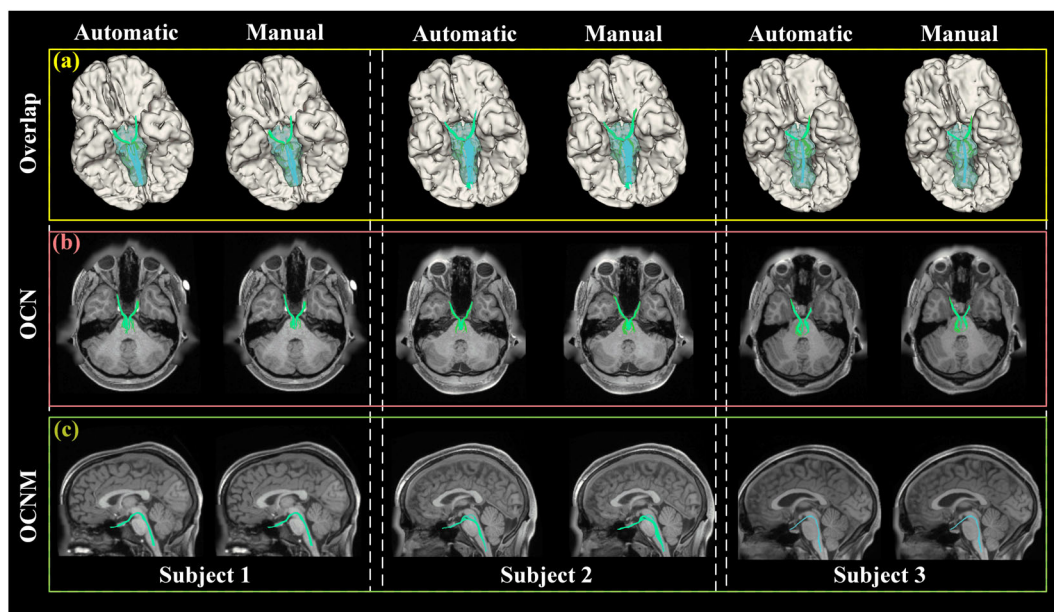


FIGURE 7 Illustration of the subdivisions of the automatic oculomotor nerve (OCN) identification. The overlap of manual and automatic methods (yellow box), OCN fibers (red box), and OCNM fibers (green box) obtained from three HCP subjects are displayed and overlaid on the T1w image. (a) Yellow box: 3D reconstruction of OCN (green), OCNM (blue), brainstem (white), and cortex (white) shown in the top row. (b) Red box: OCN fibers in the transverse plane of the T1w image. (c) Green box: OCNMs in the sagittal plane of the T1w image

demonstrate the robustness and reliability of our method in identifying OCN by using a dataset of 80 HCP subjects and 2 BSCM patients.

In tractography for individuals, we set the VentralDC and brainstem as ROI for OCN tractography because the OCN passes through the VentralDC into the cistern (Bogouslavsky, Maeder, Regli, & Meuli, 1994; Castro, Johnson, & Mamourian, 1990) and is shown to contribute to the production of OCN fibers. This operation remarkably reduces possible false-positive fibers and the working time of experts and increases the number of OCN fibers in the total fiber number of the atlas, thereby improving the possibility of creating the OCN atlas.

The proposed atlas can identify the different subdivisions of OCN. Unlike the cisternal segment of OCN that has been studied in multiple previous works, the intramesencephalic segment is relatively less studied (Tsutsumi, Miranda, Ono, & Yasumoto, 2017; Uz & Tekdemir, 2006). To our knowledge, Jang and Kwak (2017) demonstrated the possibility of identifying the putative intramesencephalic segment of OCN by using dMRI tractography. In our work, the MSMT-CSD can effectively track the intra-brainstem region. We compare the OCN tractography with combinations of multiple methods and parameters. According to our experimental results (Table 1. and Figure 5), compared to DTI and CSD, more qualified fibers can be obtained by processing data using the MSMT-CSD. DTI quantifies the dispersion of water molecules in white matter bundles in all directions by the tensor model, whose main feature direction represents the direction of white matter fiber bundle travel. However, the tensor model cannot describe the fiber crossover in the region or the tractography into the adjacent pathway, resulting in many false-positive fibers. In addition, the cisternal segment of OCN tractography

obtained through DTI is generally shorter than that obtained through MSMT-CSD because of the influence of CSF on the tensor model within the OCN voxel. The diameter of the cisternal segment of the OCN is well below the resolution achievable in DTI scans, indicating that a segment of the voxel containing the nerve is occupied by CSF (Zolal et al., 2016). When fitting the tensor model, the CSF accounts for a large proportion of the tensor model, resulting in similar eigenvalues in the spatial directions of the fitted tensor model in the region, failure to represent the OCN direction accurately, and premature stopping of tractography. In contrast to DTI and CSD, MSMT-CSD performs better based on the FOD estimation model by using multiple shells and tissues to estimate fiber directions in each voxel (Castellaro et al., 2020). Tissues respond differently with changes in b-value, and different tissues can be effectively distinguished on the basis of their different response functions (i.e., WM, GM, CSF) (Castellaro et al., 2020; Jeurissen et al., 2014). This phenomenon reduces the partial volume effect to obtain accurate fiber orientation models and explains that fibers by MSMT-CSD are clearer and more accurate than those by other two methods in the intramesencephalic segment. In the experiments on OCN reconstruction in this article, the experimental results provide a phenomenon that OCN is easier to be reconstructed than OCNM, so OCNM is equal to the overall rate. According to Figure S3, the possible reasons for this phenomenon are shown as follows: OCNM is more elongated than OCN and there is the large inflection at the intersection of the OCN-connected MLF, which is a challenge for the current tractography algorithm (Maier-Hein et al., 2017; Yang, Yeh, Poupon, & Calamante, 2021). In addition, the noise of the data will bias the FOD modeling of individual data. So, high-quality dMRI has positive effects on OCN tractography and

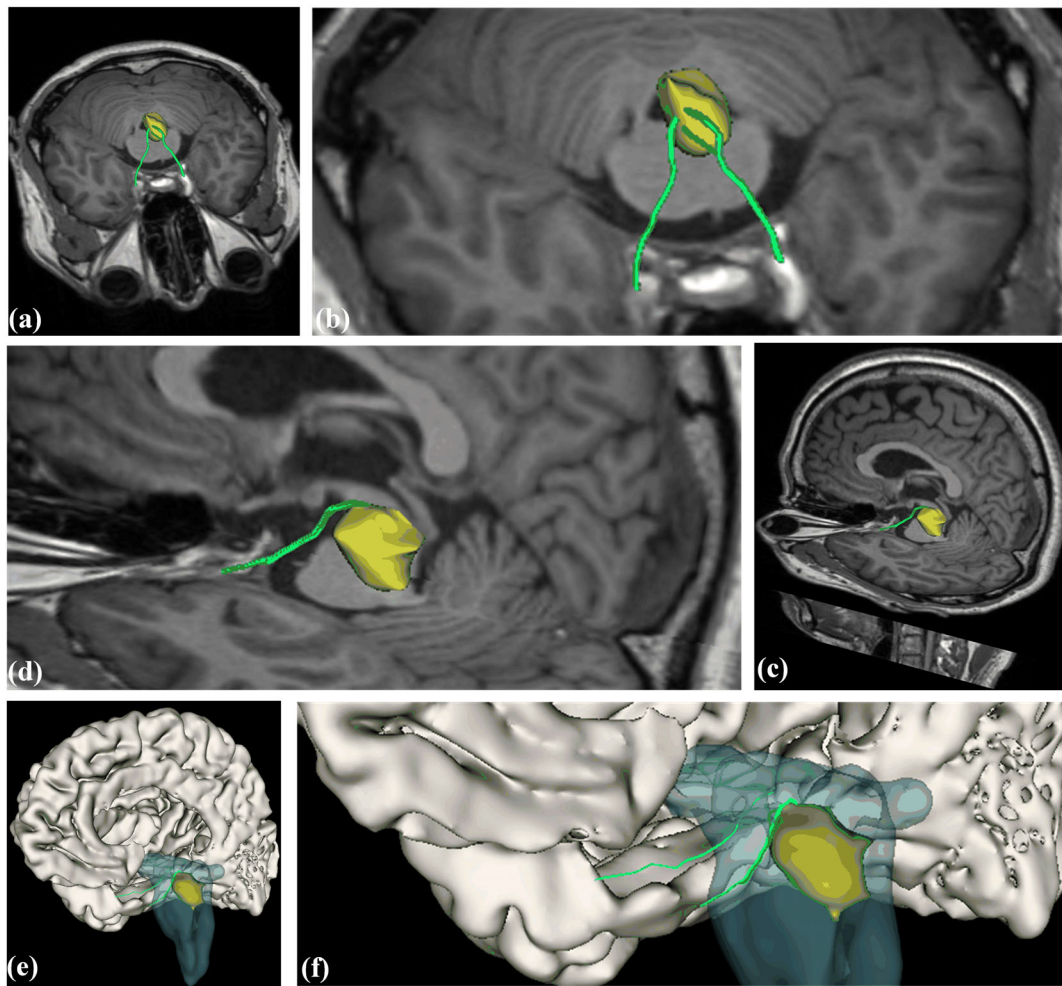


FIGURE 8 Results of automatic method in brainstem cavernous malformation (BSCM) patient data. (a) Results of automatic oculomotor nerve (OCN) identification from BSCM patient data overlaid on the transverse plane of the T1w image. (b) The details of (a). (c) Results of automatic OCN identification from BSCM patient data overlaid on the left side of the T1w image. (d) The details of (c). (e) 3D reconstruction of OCN (green), tumor (yellow), brainstem (blue), and cortex (white). (f) The details of (e)

identification (Zolal et al., 2016). For the creation of the OCN atlas, we utilize multi-shell HCP data in the present study, and the HCP dataset has minimal distortion artifacts and the highest quality.

The OCN atlas can identify different anatomical subdivisions of the OCN, where the cisternal segment of the OCN is highly visible on T1w images, and the anatomical structure is undisputed. However, the intracranial segment of the OCN is controversial because it cannot be directly reflected in structural images as follows: (a) whether the OCN is directly connected to the MLF and (b) position of the OCN to the red nuclei. First, Yeo, Jang, Kwon, and Cho (2020) and Yoshino et al. (2016) acquired fibers that connect MLF. However, according to Vitošević et al. (2013), the midbrain slice staining on the OCN shows that most of the OCN and MLF are from different sources. Moreover, OCN and MLF are close to each other, but their direct connection is not directly observed. Several scenarios result in the above findings during tractography. (a) MLF transmits motor information to the OCN through the neurotransmitter, and the OCN and MLF are close to each other. Thus, OCN and MLF blend in

periaqueductal gray. (b) The problem of the accuracy of the tractography algorithm makes it impossible to distinguish the relationship between OCN and MLF. Thus, the OCN in our work is divided into two main categories (i.e., OCN and OCNM) in accordance with anatomical differences. Second, most of OCN is medial to the caudal part of the red nucleus, less of OCN through the red nucleus itself (Castro et al., 1990; Miller et al., 1997; Vitošević et al., 2013). Moreover, OCN is close to the medial lemniscus (the outward path around the red nucleus), but all fibers converge below the red nucleus and through the interpeduncular fossa into cistern together (Miller et al., 1997; Vitošević et al., 2013). We propose that the OCN atlas contains all anatomical OCNs and classifies them completely because we choose to subdivide preprocessed brainstem fibers into 200 classes when creating the atlas, at which point the atlas successfully classifies the OCN with different anatomical subdivisions (six clusters). The 25th and 38th clusters in the atlas represent the anatomical subdivision of the OCN in the brainstem segment through the red nucleus and the medial red nucleus. The 148th and 166th clusters represent

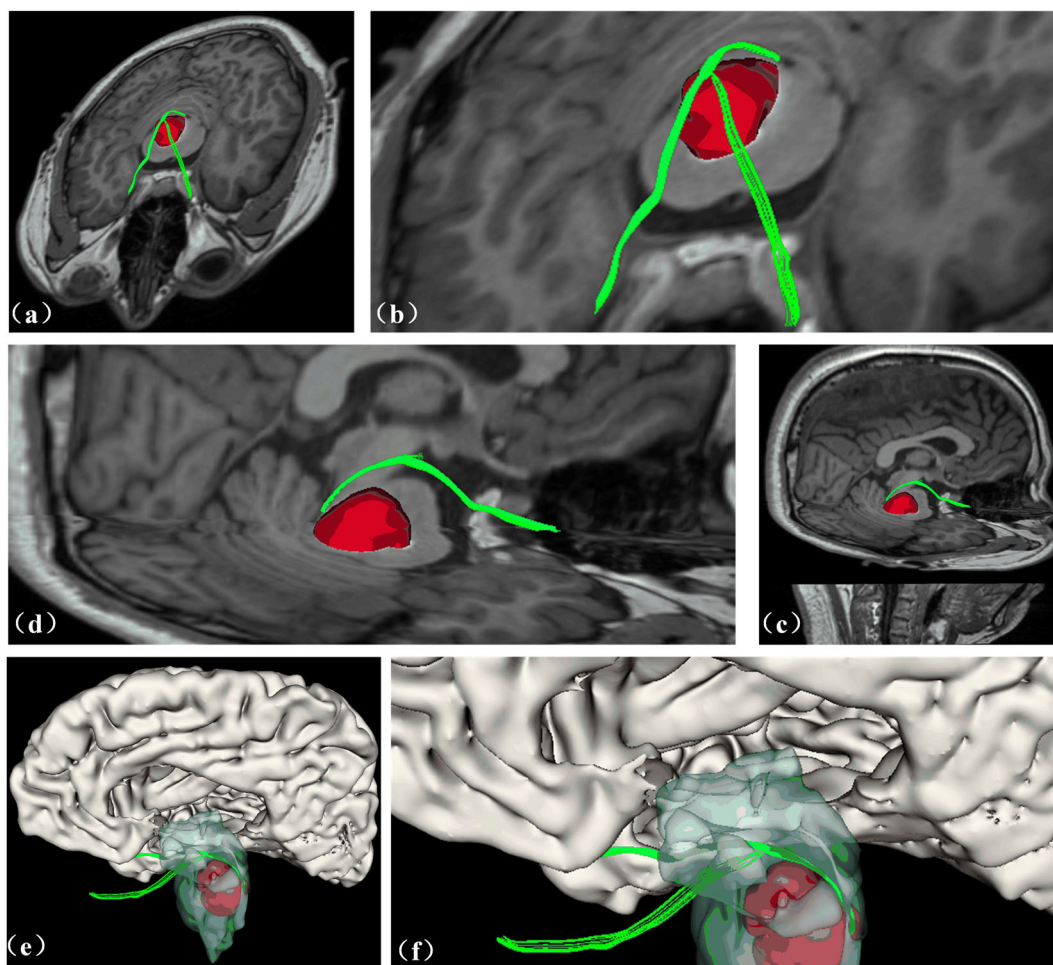


FIGURE 9 Results of automatic method in brainstem cavernous malformation (BSCM) patient data. (a) Results of automatic oculomotor nerve (OCN) identification from BSCM patient data overlaid on the transverse plane of the T1w image. (b) The details of (a). (c) Results of automatic OCN identification from BSCM patient data overlaid on the left side of the T1w image. (d) The details of (c). (e) 3D reconstruction of OCN (green), BSCM (red), brainstem (blue), and cortex (white). (f) The details of (e)

the OCN that do not pass through the red nucleus and the outer path around the red nucleus. The 71st and 177th clusters are OCNM.

In our work, we find that our proposed automatic OCN identification method has several advantages over traditional relied-on ROI methods to identify OCN fibers. First, the template of ROIs, which is used to overcome the variability, and the presence of pathology/degenerative changes across subjects still have limitations (Hodaie et al., 2010; Wedeen et al., 2008). Second, experts are unable to draw ROIs directly on structural images when the tumor occurs. Complex skull base tissues are displaced by compression and imaging artifacts and/or noise at the skull base region. In contrast to relied-on ROI methods, our method practically eliminates dependence on the manual placement of ROIs and avoids subjectivity. Moreover, the problem of multimodal data registration is avoided, and the OCN atlas identifies OCN fibers from dMRI tractography directly. Therefore, our method provides a robust tool for OCN identification.

The potential limitations of the present study, including suggested future work to address limitations, are as follows. First, we use our method to identify the OCN of subjects with different

health statuses, including healthy subjects and patients with tumor. Further evaluation can include an investigation of patients with diseases that affect OCN, for example, the relationship between the positions of OCN and blood vessel of the patient with posterior communicating aneurysms and differences in OCN between patients with diabetes and healthy subjects. Second, the orbital segment of the OCN cannot be well reconstructed at present, and our proposed method for the automatic identification of OCN does not possess an improved identification of the orbital segment of OCN. In future work, we will design methods to reconstruct the OCN pathway completely and improve our OCN atlas on the basis of our previous studies (Feng & He, 2020). Third, the proposed method performs poorly in identifying OCN that is affected by big BSCM. The mass effect of large BSCM usually leads to substantial morphological changes in OCN. Given that fiber clusters are subdivided in accordance with fiber shape and position, deformed OCN fibers may not be classified into the same cluster within the OCN atlas. In our future research, BSCM shape and the identifiers of surrounding tissues should be considered as inputs for clustering.

5 | CONCLUSION

In this study, we propose an automatic OCN identification strategy. Experimental results show that our selected tractography method and parameters are highly valuable for OCN reconstruction. The results of automatic OCN identification atlas based on dMRI tractography fibers are highly consistent with the manual OCN identification by experts. Moreover, the automatic method shows advantages over the traditional manual selection method and allows for the robust identification of different anatomical subdivisions of the OCN in the data from the different acquisitions. In the end, we successfully apply the automatic method to the data of patients with BSCM. The study provides an efficient tool for simple post-processing and reduces expert labor costs.

ACKNOWLEDGMENTS

The authors would like to thank Prof. Carl-Fredrik Westin, Prof. Lauren J. O'Donnell, Lipeng Ning PhD, and Fan Zhang PhD from Harvard Medical School for providing the method of fiber clustering software, and thank Prof. Jacques-Donald Tournier from University of Melbourne for providing his implementation for ODF reconstruction. The authors also want to thank Ye Wu PhD from University of North Carolina at Chapel Hill for experimental help.

CONFLICT OF INTEREST

The authors declare no potential conflict of interest.

DATA AVAILABILITY STATEMENT

Publicly available datasets were used in this study: Ninety diffusion MRI datasets from Human Connectome Project (HCP) database (<https://www.humanconnectome.org>) and are used in this paper. The dMRI datasets are online available. The computed tractography data will be made available on request. The data from Xuanwu Hospital that support the findings of this study are available on request from the corresponding author. The data are not publicly available due to privacy or ethical restrictions. The OCN atlas is available upon request.

ETHICS STATEMENT

All procedures performed in the studies involving human participants were in accordance with the ethical standards of the institutional and national research committee and with the 1964 Helsinki Declaration and its later amendments or comparable ethical standards.

ORCID

Jiahao Huang  <https://orcid.org/0000-0002-3866-8116>

Mengjun Li  <https://orcid.org/0000-0003-1674-9369>

Qingrun Zeng  <https://orcid.org/0000-0001-6485-8178>

REFERENCES

- Basser, P. J., Mattiello, J., & LeBihan, D. (1994). MR diffusion tensor spectroscopy and imaging. *Biophysical Journal*, *66*(1), 259–267.

- Behan, B., Chen, D. Q., Sammartino, F., DeSouza, D. D., Wharton-Shukster, E., & Hodaie, M. (2017). Comparison of diffusion-weighted MRI reconstruction methods for visualization of cranial nerves in posterior fossa surgery. *Frontiers in Neuroscience*, *11*, 554.
- Bogousslavsky, J., Maeder, P., Regli, F., & Meuli, R. (1994). Pure midbrain infarction: Clinical syndromes, MRI, and etiologic patterns. *Neurology*, *44*(11), 2032–2032.
- Bonilha, L., Gleichgerricht, E., Fridriksson, J., Rorden, C., Breedlove, J. L., Nesland, T., ... Focke, N. K. (2015). Reproducibility of the structural brain connectome derived from diffusion tensor imaging. *PLoS One*, *10*(9), e0135247.
- Brazis, P. W., Masdeu, J. C., & Biller, J. (2012). *Localization in clinical neurology*. Philadelphia: Lippincott Williams & Wilkins.
- Castellaro, M., Moretto, M., Baro, V., Brigadoi, S., Zanoletti, E., Anglani, M., ... Bertoldo, A. (2020). Multishell diffusion MRI-based tractography of the facial nerve in vestibular schwannoma. *American Journal of Neuro-radiology*, *41*(8), 1480–1486.
- Castro, O., Johnson, L. N., & Mamourian, A. C. (1990). Isolated inferior oblique paresis from brain-stem infarction: Perspective on oculomotor fascicular organization in the ventral midbrain tegmentum. *Archives of Neurology*, *47*(2), 235–237.
- Chen, D. Q., Quan, J., Guha, A., Tymianski, M., Mikulis, D., & Hodaie, M. (2011). Three-dimensional in vivo modeling of vestibular schwannomas and surrounding cranial nerves with diffusion imaging tractography. *Neurosurgery*, *68*(4), 1077–1083.
- Condos, A. (2021). Not just down and out: Oculomotor nerve pathologic spectrum. Current problems in diagnostic radiology. *Current Problems in Diagnostic Radiology*, *000*, 1–8.
- Cousineau, M., Jodoin, P. M., Garyfallidis, E., Côté, M. A., Morency, F. C., Rozanski, V., ... Descoteaux, M. (2017). A test-retest study on Parkinson's PPMI dataset yields statistically significant white matter fascicles. *NeuroImage: Clinical*, *16*, 222–233.
- Dice, L. R. (1945). Measures of the amount of ecologic association between species. *Ecology*, *26*(3), 297–302.
- Faraji, A. H., Abhinav, K., Jarbo, K., Yeh, F. C., Shin, S. S., Pathak, S., ... Friedlander, R. M. (2015). Longitudinal evaluation of corticospinal tract in patients with resected brainstem cavernous malformations using high-definition fiber tractography and diffusion connectometry analysis: Preliminary experience. *Journal of Neurosurgery*, *123*(5), 1133–1144.
- Feng, Y., & He, J. (2020). Asymmetric fiber trajectory distribution estimation using streamline differential equation. *Medical Image Analysis*, *63*, 101686.
- Fischl, B. (2012). FreeSurfer. *Neuroimage*, *62*(2), 774–781.
- Fowlkes, C., Belongie, S., Chung, F., & Malik, J. (2004). Spectral grouping using the Nystrom method. *IEEE Transactions on Pattern Analysis and Machine Intelligence*, *26*(2), 214–225.
- Glasser, M. F., Sotiropoulos, S. N., Wilson, J. A., Coalson, T. S., Fischl, B., Andersson, J. L., Xu, J., Jbabdi, S., Webster, M., R. Polimeni, J., Essen, D. C. V., Jenkinson, M., & Wu-Minn HCP Consortium. (2013). The minimal preprocessing pipelines for the human connectome project. *NeuroImage*, *80*, 105–124.
- Gong, G., He, Y., Concha, L., Lebel, C., Gross, D. W., Evans, A. C., & Beaulieu, C. (2009). Mapping anatomical connectivity patterns of human cerebral cortex using in vivo diffusion tensor imaging tractography. *Cerebral Cortex*, *19*(3), 524–536.
- Guevara, M., Román, C., Houenou, J., Duclap, D., Poupon, C., Mangin, J. F., & Guevara, P. (2016). *Creation of a whole brain short association bundle atlas using a hybrid approach*. 2016 38th Annual International Conference of the IEEE Engineering in Medicine and Biology Society (EMBC). IEEE. pp. 1115–1119.
- He, J., Zhang, F., Xie, G., Yao, S., Feng, Y., Bastos, D. C. A., ... O'Donnell, L. J. (2021). Comparison of multiple tractography methods for reconstruction of the retinogeniculate visual pathway using diffusion MRI. *Human Brain Mapping*, *42*(12), 3887–3904.

- Hodaie, M., Quan, J., & Chen, D. Q. (2010). In vivo visualization of cranial nerve pathways in humans using diffusion-based tractography. *Neurosurgery*, 66(4), 788–796.
- Inoue, H., Hashiguchi, A., Moroki, K., & Tokuda, H. (2020). Unruptured internal carotid-posterior communicating artery aneurysm splitting the oculomotor nerve: A case report and literature review. *Surgical Neurology International*, 11(353), 1–3.
- Jacquesson, T., Frindel, C., Kocivar, G., Berhouma, M., Jouanneau, E., Attyé, A., & Cotton, F. (2019). Overcoming challenges of cranial nerve tractography: A targeted review. *Neurosurgery*, 84(2), 313–325.
- Jacquesson, T., Yeh, F. C., Panesar, S., Barrios, J., Attyé, A., Frindel, C., ... Fernandez-Miranda, J. C. (2019). Full tractography for detecting the position of cranial nerves in preoperative planning for skull base surgery. *Journal of Neurosurgery*, 132(5), 1642–1652.
- Jang, S., & Kwak, S. (2017). Diffusion tensor tractography for determining injury to the oculomotor nerve in a patient with cerebral infarct. *Annals of Rehabilitation Medicine*, 41(4), 720.
- Jeurissen, B., Tournier, J. D., Dhollander, T., Connelly, A., & Sijbers, J. (2014). Multi-tissue constrained spherical deconvolution for improved analysis of multi-shell diffusion MRI data. *NeuroImage*, 103, 411–426.
- Kwon, H. G., Kim, M. S., Kim, S. H., & Jang, S. H. (2013). Injury of the oculomotor nerve in a patient with traumatic brain injury: Diffusion tensor tractography study. *Journal of Neurology, Neurosurgery & Psychiatry*, 84(10), 1073–1074.
- Lazar, M., Alexander, A. L., Thottakara, P. J., Badie, B., & Field, A. S. (2006). White matter reorganization after surgical resection of brain tumors and vascular malformations. *American Journal of Neuroradiology*, 27(6), 1258–1271.
- Li, D., Jiao, Y. M., Wang, L., Lin, F. X., Wu, J., Tong, X. Z., ... Cao, Y. (2018). Surgical outcome of motor deficits and neurological status in brainstem cavernous malformations based on preoperative diffusion tensor imaging: A prospective randomized clinical trial. *Journal of Neurosurgery*, 130(1), 286–301.
- Li, M., Yeh, F. C., Zeng, Q., Wu, X., Wang, X., Zhu, Z., ... Li, M. (2021). The trajectory of the medial longitudinal fasciculus in the human brain: A diffusion imaging based tractography study. *Human Brain Mapping*, 42, 6070–6080.
- Liang, C., Du, Y., Lin, X., Wu, L., Wu, D., & Wang, X. (2009). Anatomical features of the cisternal segment of the oculomotor nerve: Neurovascular relationships and abnormal compression on magnetic resonance imaging. *Journal of Neurosurgery*, 111(6), 1193–1200.
- Maier-Hein, K. H., Neher, P. F., Houde, J. C., Côté, M. A., Garyfallidis, E., Zhong, J., ... Descoteaux, M. (2017). The challenge of mapping the human connectome based on diffusion tractography. *Nature Communications*, 8(1), 1–13.
- Malinsky, M., Peter, R., Hodneland, E., Lundervold, A. J., Lundervold, A., & Jan, J. (2013). Registration of FA and T1-weighted MRI data of healthy human brain based on template matching and normalized cross-correlation. *Journal of Digital Imaging*, 26(4), 774–785.
- Miller, M. J., Mark, L. P., Ho, K. C., & Haughton, V. M. (1997). Anatomic relationship of the oculomotor nuclear complex and medial longitudinal fasciculus in the midbrain. *American Journal of Neuroradiology*, 18(1), 111–113.
- Muhammad, S., & Niemelä, M. (2019). Management of oculomotor nerve schwannoma: Systematic review of literature and illustrative case. *Surgical Neurology International*, 10(40), 1–6.
- Nakagawa, Y., Toda, M., Shibao, S., & Yoshida, K. (2017). Delayed and isolated oculomotor nerve palsy following minor head trauma. *Surgical Neurology International*, 8, 20.
- O'Donnell, L. J., Suter, Y., Rigolo, L., Kahali, P., Zhang, F., Norton, I., ... Golby, A. J. (2017). Automated white matter fiber tract identification in patients with brain tumors. *NeuroImage: Clinical*, 13, 138–153.
- O'Donnell, L. J., Wells, W. M., Golby, A. J., & Westin, C. F. (2012). *Unbiased groupwise registration of white matter tractography*. International Conference on Medical Image Computing and Computer-Assisted Intervention. Berlin, Heidelberg: Springer. pp. 123–130.
- O'Donnell, L. J., & Westin, C. F. (2007). Automatic tractography segmentation using a high-dimensional white matter atlas. *IEEE Transactions on Medical Imaging*, 26(11), 1562–1575.
- Park, H. K., Rha, H. K., Lee, K. J., Chough, C. K., & Joo, W. (2017). Microsurgical anatomy of the oculomotor nerve. *Clinical Anatomy*, 30(1), 21–31.
- Presseau, C., Jodoin, P. M., Houde, J. C., & Descoteaux, M. (2015). A new compression format for fiber tracking datasets. *NeuroImage*, 109, 73–83.
- Sporns, O., Tononi, G., & Kötter, R. (2005). The human connectome: A structural description of the human brain. *PLoS Computational Biology*, 1(4), e42.
- Sultana, S. (2017). *Development of an atlas-based segmentation of cranial nerves using shape-aware discrete deformable models for neurosurgical planning and simulation*. Norfolk, England: Old Dominion University.
- Taha, A. A., & Hanbury, A. (2015). Metrics for evaluating 3D medical image segmentation: Analysis, selection, and tool. *BMC Medical Imaging*, 15(1), 1–28.
- Tam, E. K., Lonngi, M., & Demer, J. L. (2018). MRI findings of contralateral oculomotor nerve palsy in Parry-Romberg syndrome. *American Journal of Ophthalmology Case Reports*, 10, 81–83.
- Taniguchi, M., Nakai, T., Kimura, H., Fujita, Y., Uozumi, Y., Kohta, M., & Kohmura, E. (2018). Endoscopic endonasal surgery for pituitary adenomas extending to the oculomotor cistern. *Head & Neck*, 40(3), 536–543.
- Tournier, J. D., Calamante, F., & Connelly, A. (2012). MRtrix: Diffusion tractography in crossing fiber regions. *International Journal of Imaging Systems and Technology*, 22(1), 53–66.
- Tournier, J. D., Smith, R., Raffelt, D., Tabbara, R., Dhollander, T., Pietsch, M., ... Connelly, A. (2019). MRtrix3: A fast, flexible and open software framework for medical image processing and visualisation. *NeuroImage*, 202, 116137.
- Tsutsumi, S., Miranda, J. C. F., Ono, H., & Yasumoto, Y. (2017). The cisternal segments of the oculomotor nerve: A magnetic resonance imaging study. *Surgical and Radiologic Anatomy*, 39(3), 323–331.
- Uz, A., & Tekdemir, I. (2006). Relationship between the posterior cerebral artery and the cisternal segment of the oculomotor nerve. *Journal of Clinical Neuroscience*, 13(10), 1019–1022.
- Van Essen, D. C., Smith, S. M., Barch, D. M., Behrens, T. E., Yacoub, E., Ugurbil, K., & Wu-Minn HCP Consortium. (2013). The WU-Minn human connectome project: An overview. *NeuroImage*, 80, 62–79.
- Vitošević, Z., Marinković, S., Četković, M., Štimec, B., Todorović, V., Kanjuh, V., & Milisavljević, M. (2013). Intramesencephalic course of the oculomotor nerve fibers: Microanatomy and possible clinical significance. *Anatomical Science International*, 88(2), 70–82.
- Wassermann, D., Makris, N., Rathi, Y., Shenton, M., Kikinis, R., Kubicki, M., & Westin, C. F. (2016). The white matter query language: A novel approach for describing human white matter anatomy. *Brain Structure and Function*, 221(9), 4705–4721.
- Wedeen, V. J., Wang, R. P., Schmahmann, J. D., Benner, T., Tseng, W. Y. I., Dai, G., ... de Crespigny, A. J. (2008). Diffusion spectrum magnetic resonance imaging (DSI) tractography of crossing fibers. *NeuroImage*, 41(4), 1267–1277.
- Wu, Y., Zhang, F., Makris, N., Ning, Y., Norton, I., She, S., ... O'Donnell, L. J. (2018). Investigation into local white matter abnormality in emotional processing and sensorimotor areas using an automatically annotated fiber clustering in major depressive disorder. *NeuroImage*, 181, 16–29.
- Xie, G., Zhang, F., Leung, L., Mooney, M. A., Epprecht, L., Norton, I., ... O'Donnell, L. J. (2020). Anatomical assessment of trigeminal nerve tractography using diffusion MRI: A comparison of acquisition b-values and single-and multi-fiber tracking strategies. *NeuroImage: Clinical*, 25, 102160.

- Yang, H. K., Kim, J. H., & Hwang, J. M. (2020). Magnetic resonance imaging in 14 patients with congenital oculomotor nerve palsy. *Clinical Neuro-radiology*, 30(2), 237–242.
- Yang, J. Y. M., Yeh, C. H., Poupon, C., & Calamante, F. (2021). Diffusion MRI tractography for neurosurgery: The basics, current state, technical reliability and challenges. *Physics in Medicine & Biology*, 66, 15TR01.
- Yeo, S. S., Jang, S. H., Kwon, J. W., & Cho, I. H. (2020). Three-dimensional identification of the medial longitudinal fasciculus in the human brain: A diffusion tensor imaging study. *Journal of Clinical Medicine*, 9(5), 1340.
- Yoshino, M., Abhinav, K., Yeh, F. C., Panesar, S., Fernandes, D., Pathak, S., ... Fernandez-Miranda, J. C. (2016). Visualization of cranial nerves using high-definition fiber tractography. *Neurosurgery*, 79(1), 146–165.
- Zeng, Q., Li, M., Yuan, S., He, J., Wang, J., Chen, Z., ... Feng, Y. (2021). Automated facial-vestibulocochlear nerve complex identification based on data-driven tractography clustering. *NMR in Biomedicine*, 34(12), e4607.
- Zhang, F., Xie, G., Leung, L., Mooney, M. A., Epprecht, L., Norton, I., ... O'Donnell, L. J. (2020). Creation of a novel trigeminal tractography atlas for automated trigeminal nerve identification. *NeuroImage*, 220, 117063.
- Zhao, J., Li, Y., Chang, Q., Wang, J., & Sun, H. (2021). Diabetic oculomotor nerve palsy displaying enhancement of the oculomotor nerve in the orbit and cavernous sinus on MRI. *European Neurology*, 84(8), 1–8.
- Zolal, A., Sobottka, S. B., Podlesek, D., Linn, J., Rieger, B., Juratli, T. A., ... Kitzler, H. H. (2016). Comparison of probabilistic and deterministic fiber tracking of cranial nerves. *Journal of Neurosurgery*, 127(3), 613–621.

SUPPORTING INFORMATION

Additional supporting information may be found in the online version of the article at the publisher's website.

How to cite this article: Huang, J., Li, M., Zeng, Q., Xie, L., He, J., Chen, G., Liang, J., Li, M., & Feng, Y. (2022). Automatic oculomotor nerve identification based on data-driven fiber clustering. *Human Brain Mapping*, 43(7), 2164–2180. <https://doi.org/10.1002/hbm.25779>